ACS Photonics

pubs.acs.org/journal/apchd5

Letter

Lasing from Finite Plasmonic Nanoparticle Lattices

Danqing Wang, Marc R. Bourgeois, Jun Guan, Ahmad K. Fumani, George C. Schatz,* and Teri W. Odom*

Cite This: *ACS Photonics* 2020, 7, 630–636

Read Online

ACCESS | Metrics & More | Article Recommendations | Supporting Information

ABSTRACT: Small lasers can generate coherent light for integrated photonics, *in vivo* cellular imaging, and solid-state lighting. Unlike conventional lasers, plasmonic lasers can generate coherent light at subwavelength scales, although cavity architectures based on metal films and semiconducting gain exhibit large radiative losses and lack directional emission. In contrast, 2D metal nanoparticle arrays surrounded by organic dyes can support lasing with high directionality at room temperature. However, the relationship between the number of nanoparticles in a finite lattice and their lasing emission characteristics is unknown. Here we show that the number of units in 2D gold nanoparticle lattices is critical to generate robust cavity resonances and lasing emission. Narrower lattice plasmons associated with stronger electromagnetic near fields are observed as the nanoparticle number increases. Experimentally, we demonstrate lasing from a 30 × 30 nanoparticle lattice. Semiquantum modeling indicates lower lasing thresholds and faster population inversion dynamics with higher nanoparticle numbers. These results suggest that finite lattices of nanoparticles integrated with gain can function as independent, coherent light sources for optical multiplexing and lab-on-a-chip applications.

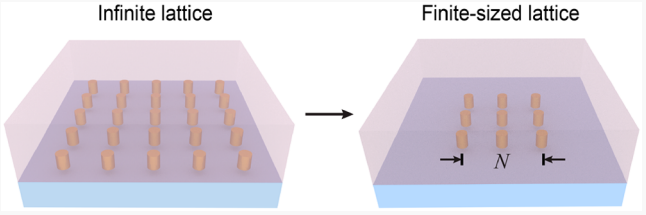

KEYWORDS: *metal nanoparticle lattices, small lasers, finite size, lattice plasmons, surface lattice resonances*

Rationally assembled nanostructures with metal nanoparticles (NPs) as building blocks exhibit distinct collective optical properties. Single NPs support broad localized surface plasmons (LSPs, full-width-at-half-maximum, fwhm >100 nm) that depend on shape, size, and materials of the particles.[1−3] For dimers of two closely spaced metal NPs, a gap mode with electromagnetic fields confined between the NPs is excited when the polarization of incident light is along the long axis of the dimer.[4,5] More complex assemblies of three or more plasmonic NPs can access high-order modes and magnetic resonances with distinct near-field distributions depending on the overall geometry.[6,7] In a periodic 2D lattice, metal NPs can be diffractively coupled when they are separated by the wavelength of light.[8,9] The ultrasharp (fwhm <5 nm) and strong lattice plasmon resonances (also referred to as surface lattice resonances) originate from coupling of the LSPs of the NPs to diffraction modes defined by the lattice.[9−11] Strongly enhanced electromagnetic fields confined to the subwavelength vicinity of the NPs are critical for light−matter interactions, from nonlinear optics to lasing to quantum optics.[11−13]

Finite-size effects are important in determining the optical properties of nanostructures. For example, finite-area nanohole arrays in plasmonic films show extraordinary optical transmission and broadband lensing.[14,15] In 1D distributed feedback lasers, the emission line width $\Delta\lambda$ is related to the total unit number N by $\Delta\lambda \propto 1/N$.[16,17] Two-dimensional metal NP lattices integrated with gain media can support lasing emission with high directionality and spectral tunability.[18−21] Most work has focused on the scaling up (cm^2) of lattice plasmon lasers based on advances in nanofabrication to create the cavity structures, but miniaturized photonics favors smaller footprints.[22,23] Although lasing has been observed from a microscale 2D NP array,[24] the dependence of lasing output characteristics on NP number in finite lattices is unknown.

Here we report the lower bound of NP number in a finite 2D lattice that can show robust lattice plasmon resonances and lasing action. By increasing the total NP number N, we observed narrower dipolar lattice plasmons associated with stronger optical near fields. Coupled dipole calculations revealed that the induced dipole moments are enhanced at the lattice edges along the incident light polarization direction; the distribution of dipole moments across the lattice is sensitive to N and NP diameter d. As a general trend, we found that the mode quality of a finite lattice gradually approached that of an infinite lattice with increased N, and the required critical value of N is higher for lattices with smaller NPs. Lasing was observed from a 30 × 30 NP lattice in experiment. Semiquantum modeling showed that with increased NP number, the stronger optical near fields led to faster population inversion buildup and more intense lasing emission.

Received: February 12, 2020
Published: February 24, 2020

https://dx.doi.org/10.1021/acsphotonics.0c00231
ACS Photonics 2020, 7, 630−636

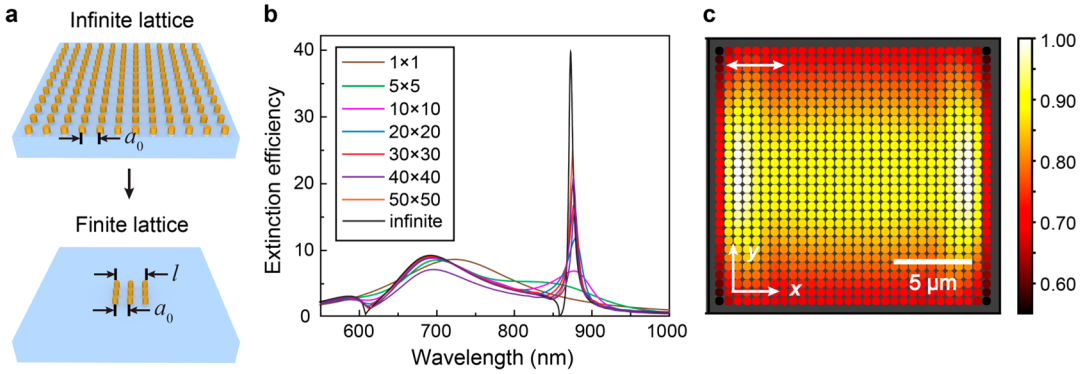

Figure 1. Coupled dipole approximation modeling of a finite nanoparticle (NP) lattice shows more intense and narrower lattice plasmon resonances with increased NP number. (a) Scheme showing infinite and finite NP arrays. (b) Dependence of extinction spectra on NP number N in a finite 2D lattice from the coupled dipole method for gold NP lattices with spacing a_0 = 600 nm, NP diameter d = 130 nm, and height h = 50 nm. The background refractive index was n = 1.43. (c) Spatial map of the magnitude of the induced dipole moment at each NP site showing edge effects in a 30 × 30 NP lattice. The white arrow on top denotes polarization direction of the incident light.

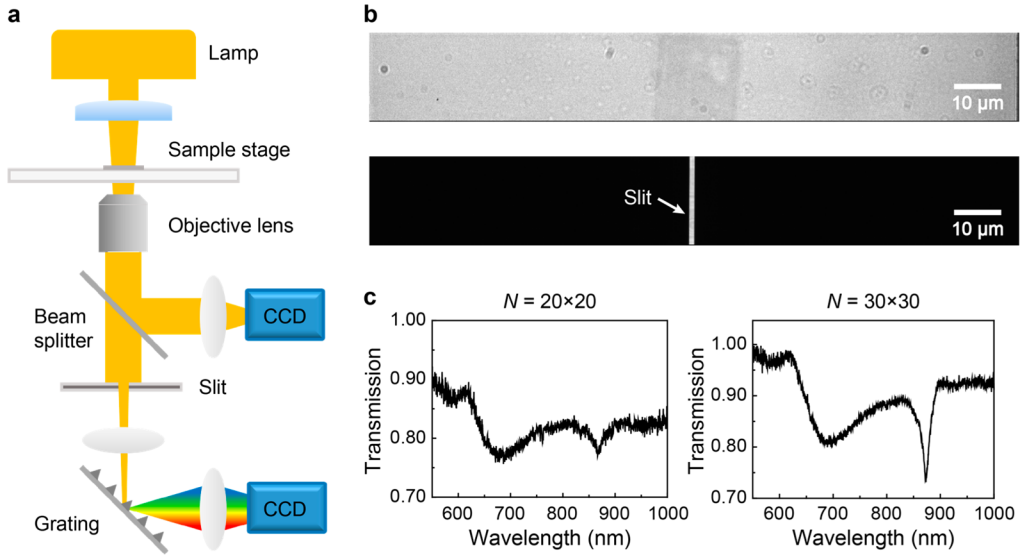

Figure 2. Measured linear optical properties of finite gold NP lattices showed narrowed lattice plasmons with increased nanoparticle number. (a) Optical setup of a dark-field microscope for imaging and spectroscopy. (b) Image of a finite NP lattice under the microscope with side length l = 18 μm, NP spacing a_0 = 600 nm, diameter d = 130 nm, and height h = 50 nm (upper panel). The central gray area shows the finite NP lattice in the field of view. Lower panel shows the same lattice with an inserted slit. (c) Measured transmission spectra from finite lattices with varying NP number N from 20 × 20 to 30 × 30.

Figure 1 illustrates the narrowing of lattice plasmon resonances with increased NP number N calculated with the coupled dipole approximation (CDA) method, where large numbers of NPs can be included with low computational cost.[9,25−27] We used a home-built code based on CDA to model finite and infinite 2D lattices with numerically calculated cylindrical NP polarizability tensors and site-dependent dipole moments for NPs (Figure 1a, Methods). In the infinite-lattice limit, the lattice plasmon wavelength is determined by the intersection between the real parts of the lattice sum S determined by the array geometry and the inverse of the NP polarizability ($1/\alpha_{NP}$); the resonance line width is governed by the imaginary part of $1/\alpha_{NP} - S$.[27] The resonance mode quality ($Q \approx \lambda/\Delta\lambda$) of lattice plasmons in an infinite lattice is sensitive to NP size, lattice spacing, and NP materials.[9] Compared to larger ones, smaller NPs sustain less radiative damping, which results in lattice plasmons that blue-shift toward the Rayleigh anomaly with increased mode quality (Figure S1a).[27]

For a fixed NP diameter d = 130 nm and height h = 50 nm, CDA calculations show a broad LSP resonance with line width $\Delta\lambda$ = 160.8 nm. As N increases from 10 × 10 to 50 × 50 in a finite lattice (a_0 = 600 nm), the resonance line width reduces from $\Delta\lambda$ = 34.7 nm to $\Delta\lambda$ = 7.8 nm until gradually saturating at the infinite-lattice line width ($\Delta\lambda$ = 6.5 nm) (Figure 1b). Calculations for varying N and NP diameter d reveal that NP size influences how rapidly the line widths of finite lattices approach that of an infinite lattice (Figures S2 and S3). Although infinite lattices with smaller NPs support SLRs with higher quality than those composed of larger NPs, finite lattices of smaller NPs require higher N to converge to this limit (Figure S1b). This dependence can be understood by noting that the radiative losses associated with larger NPs limit the mode quality while facilitating stronger far-field coupling to other NPs in the finite lattice. In contrast, smaller NPs scatter light less efficiently and require a larger number of NPs with in-phase interactions to approach the infinite-lattice limit (Figure S1b). Similar trends with NP size and the number of NPs in

https://dx.doi.org/10.1021/acsphotonics.0c00231
ACS Photonics 2020, 7, 630−636

finite lattices were observed recently based on CDA in the context of near-field enhancements.[28] Compared to the CDA method, finite-difference time-domain (FDTD) simulations can capture contributions from high-order resonances beyond dipolar plasmons. FDTD simulations of arrays of large gold NPs (d = 260 nm, h = 120 nm) indicate that lattice plasmons mediated by hybrid quadrupolar modes[29] show a similar dependence on NP number. The resonance intensity of hybrid quadrupolar lattice plasmons is stronger and with narrower line widths for a finite lattice as N increases from 10 × 10 to 30 × 30 NPs (Figure S4).

Although the dipole moments supported at each NP site for an infinite lattice are identical, the induced moments in a finite lattice vary spatially due to the reduced symmetry environment near the lattice edges. CDA calculations for finite lattices with NP diameter d = 130 nm show that the magnitudes of induced dipole moments are largest at the lattice edges along the direction of the incident light polarization (x) and are confined at the center along the perpendicular direction (y) (Figure 1c). As N increases, the distribution of dipole moments along x evolves to be more uniform, and the distribution along y narrows toward the lattice center (Figure S5a). Consistent with the CDA results, FDTD simulations on the optical near fields show orders of magnitude enhancement (from $|\mathbf{E}|^2/|\mathbf{E}_0|^2$ = 50 to $|\mathbf{E}|^2/|\mathbf{E}_0|^2$ = 800) at the lattice center as N increases from 1 to 50 × 50 and approach the infinite lattice case for more than 50 × 50 NPs (Figure S6). Interestingly, the evolution of dipole moment distributions appears to follow a general trend connected to the mode quality (Figure S1). Once N approaches the regime where the quality factor Q plateaus, as evident for large NPs (d = 160 nm), the dipole moment distribution among NPs becomes uniform along x. In contrast, the induced dipole moments are no longer confined at the lattice center along y, and the peak positions move toward the lattice edges with increased N (Figure S5b,c).

On the basis of multiscale nanopatterning techniques,[30] we fabricated finite NP lattices with different overall lattice sizes (l = 12, 18 μm) and large spacings in between. We measured the normal incidence, zero-order transmission of finite lattices to characterize how the lattice resonance line width and intensity changed with increased NP number. The optical measurement was adapted from a dark-field microscope by removing the condenser lens to allow incident light to be perpendicular to the sample (Figure 2a). The transmitted light from a finite NP lattice was collected by a high-numerical-aperture (NA) objective lens (100×) before focusing onto the camera. A narrow slit before the detector ensured that the transmission collected from the NP lattices was from the surface normal and not from dispersive propagating lattice modes at oblique angles (Figure 2b). The measured lattice plasmons show reduced resonance line width $\Delta\lambda$ and enhanced resonance depth as N increased from 20 × 20 to 30 × 30 (Figure 2c), consistent with the CDA results. With more NPs in the lattice, the intensity of the LSPs (~680 nm) was also stronger. The higher quality factor Q from the reduced line width $\Delta\lambda$ indicates that photons can be trapped within the cavity for more cycles with increased N. Notably, gold and silver NP lattices support high-quality lattice plasmons at near-infrared wavelengths because of their small imaginary parts of the permittivity.[9] The relatively strong near fields ($|\mathbf{E}|^2/|\mathbf{E}_0|^2$ > 300) for a 30 × 30 gold NP lattice in this work are comparable to that of a near-infinite aluminum NP lattice with the same NP size and spacing.[31]

Nanolasing devices consisted of finite NP lattices on fused silica surrounded by liquid dye IR-140 (dissolved in dimethyl sulfoxide) kept in place with a glass cover slide (Figure 3a). We

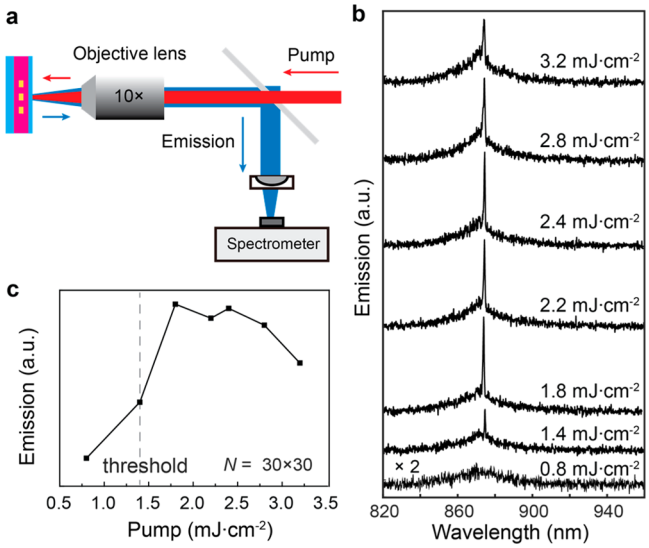

Figure 3. Lasing action from a finite lattice of gold NPs at room temperature. (a) Optical setup with objective lens for beam focusing and detection. (b) Measured single-mode lasing from a 30 × 30 NP lattice with lattice size l = 18 μm, NP diameter d = 130 nm, and height h = 50 nm. (c) Input−output curves for the finite NP lattice. The concentration of dye IR-140 is C = 1 mM.

used an objective lens (10×) to focus an 800 nm fs-pulsed laser beam to the microscale lattice region (spot diameter ~30 μm). The large spacing (180 μm) between the finite lattices ensured that only a single lattice was exposed and detected within the field of view of the lens. We observed single-mode lasing emission (line width ~0.5 nm) from a 30 × 30 gold NP lattice with dye concentration C = 1 mM at room temperature (Figure 3b). The lasing threshold (1.4 mJ/cm^2) was around 1 order of magnitude higher than that of an infinite lattice with similar dye concentration,[20] consistent with the relatively lower mode quality and weaker near fields of a finite lattice (Figures S6). Similar to infinite NP lattices that showed saturation of lasing intensity at high pump powers,[32] the emission intensity of a finite lattice reached a plateau for pump powers over 1.8 mJ/cm^2 and decreased above 2.4 mJ/cm^2. This decrease may originate from additional energy dissipation channels through amplified spontaneous emission[32] at oblique angles (Figure 3c). Compared to the report of lasing from both bright and dark modes in finite lattices,[24] we did not observe lasing from dark modes possibly because of the different NP materials (gold instead of silver) and low dye concentrations (1 mM compared to 30 mM) in our system.

We exploited semiquantum modeling with a time-domain approach to study the dependence of lasing emission intensity and buildup dynamics on NP number (Figure 4a). The unit supercell consists of a finite gold NP lattice embedded in organic dye solvent and a pulsed pump normal to the lattice plane (Figure S7). Only when the 2D lattices exceeded 30 × 30 NPs was single-mode lasing observed at the monitor plane with characteristic time-dependent population inversion (dye concentration C = 1 mM, pump power 0.9 mJ/cm^2) (Figure 4b). Based on the semiquantum model,[29] the near-field $\mathbf{E}$ around the NPs enhances the stimulated emission rate

https://dx.doi.org/10.1021/acsphotonics.0c00231
ACS Photonics 2020, 7, 630−636

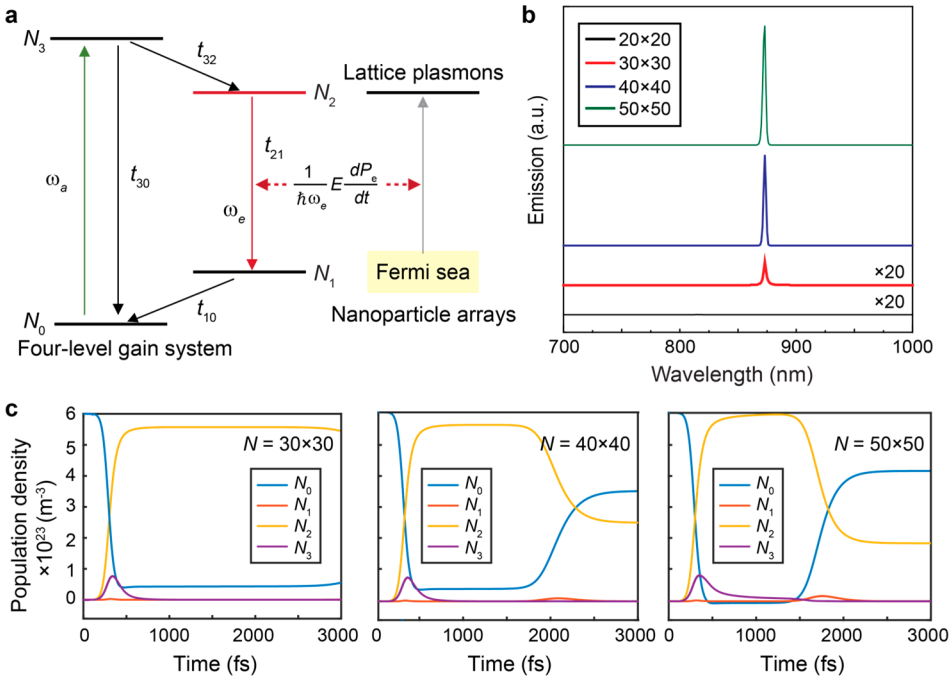

Figure 4. Semiquantum modeling with a time-domain approach reveals that lasing emission intensity and ultrafast dynamics depend strongly on NP number. (a) Scheme showing the semiquantum system for modeling the energy transfer process between the four-level dye system and lattice plasmon resonances. N_i represents the population density and P_e denotes the net macroscopic polarization. ω_a and ω_e are absorption and emission frequencies, respectively. (b) N-dependent lasing emission under a pump power of 0.9 mJ/cm^2 and dye concentration C = 1 mM. Gold NPs had a diameter d = 130 nm, height h = 50 nm, and lattice spacing a_0 = 600 nm. (c) Time-dependent population inversion with different N.

$(\frac{1}{\hbar w}\mathbf{E}\frac{\mathrm{d}\mathbf{P}}{\mathrm{d}t})$ by a factor of $\mathbf{E}^2$; hence, the stronger near fields for finite lattices with higher N resulted in faster population inversion buildup and stronger lasing emission (Figure 4c). In addition, the modeled lasing from finite NP lattices showed threshold behavior and intensity saturation at high powers, consistent with experiments (Figure S8). Besides cavity mode quality, we note that the lasing threshold is also sensitive to dye concentration, decay lifetime, and spectral overlap between the cavity resonance position and gain emission envelope. Increased dye concentration or reduced decay lifetime t_{21} induced faster lasing buildup and stronger lasing emission (Figures S9, S10). Hence, under a fixed pump power, dye concentration can function as a probe of cavity losses in finite NP lattices.

In conclusion, we experimentally identified and theoretically confirmed the critical NP number in finite plasmonic lattices needed to approach the lasing characteristics from infinite lattices. The accurate evaluation of lattice sums and NP polarizabilities with the CDA method enables a reliable comparison between near-infinite and finite lattice systems. Our findings indicate that lasing from finite NP lattices (tens of micrometers on one side) can function as independent, coherent light sources for lab-on-a-chip applications. For example, multiplexed optical systems are possible with finite lattices as modular elements, where different-spaced finite lattices and various gain materials could enable multicolor lasing emission at red, green, and blue wavelengths. We expect that such small-footprint lasers can be integrated within cellular environments for *in vivo* imaging, diagnostic, and therapeutic applications.

METHODS

Fabrication of Finite Gold NP Lattices. Finite lattices of gold NPs on fused silica were fabricated with a large-scale nanofabrication process known as PEEL.[30] Briefly, we generated periodic arrays of photoresist posts on a Si wafer by phase-shifting photolithography. A poly(dimethylsiloxane) (PDMS) mask with post periodicity a_0 = 600 nm was used for phase-shifting photolithography, and Cr masks with different lattice side length l = 6 μm, 12 μm, and 18 μm and large separations were used for contact photolithography. The photoresist post patterns were then transferred into free-standing gold nanohole films after Cr deposition, removal of photoresist posts, etching through the Si, and lift-off of the gold film. Finally, we created gold NP arrays by metal deposition through the hole-array mask on fused silica and then removal of the mask with Scotch tape.

Coupled Dipole Modeling. Within the coupled dipole approximation, the normalized finite-lattice extinction efficiency associated with a plane-wave incident field is

$$\sigma_{\mathrm{ext}}^{\mathrm{finite}} = \frac{k}{\pi R^2 \varepsilon_r \varepsilon_0 |E_0|^2} \mathrm{Im}\left\{\sum_{i=1}^{N} \mathbf{E}_0^*(r_i)\cdot\mathbf{p}_i\right\}$$

where k is the wave vector of the incident field, R is the cylinder radius, and $\mathbf{E}_0$ is the incident plane wave field. The dipole moment $\mathbf{p}_i$ induced at each lattice site is found by solving the linear system of coupled equations

$$\mathbf{p}_i = \vec{\alpha}_i \cdot \left(\mathbf{E}_0(\mathbf{r}_i) + \frac{k^2}{\varepsilon_r \varepsilon_0} \sum_{j\neq i}^{N} \vec{\mathbf{G}}(\mathbf{r}_i, \mathbf{r}_j, \omega)\cdot\mathbf{p}_j\right)$$

where $\vec{\alpha}_i$ is the polarizability tensor characterizing the dipolar response of each NP and $\vec{\mathbf{G}}$ is the Greens dyadic given by

https://dx.doi.org/10.1021/acsphotonics.0c00231
ACS Photonics 2020, 7, 630−636

$$\vec{\mathbf{G}}(r_i, r_j, \omega) = \left[\left(1 + \frac{i}{kR_{ij}} - \frac{1}{(kR_{ij})^2}\right)\vec{\mathbf{I}} + \left(-1 - \frac{3i}{kR_{ij}} + \frac{3}{(kR_{ij})^2}\right)\hat{\mathbf{R}}_{ij}\hat{\mathbf{R}}_{ij}\right]\frac{e^{ikR_{ij}}}{4\pi R_{ij}}$$

where $R_{ij} = |\mathbf{r}_i - \mathbf{r}_j|$, $\hat{\mathbf{R}}_{ij} = r_i - r_j/R_{ij}$, and $\hat{\mathbf{R}}_{ij}\hat{\mathbf{R}}_{ij}$ represents the dyadic product.

The infinite-lattice extinction is given by

$$\sigma_{\text{ext}}^{\text{infinite}} = \frac{k}{\pi R^2 \varepsilon_r \varepsilon_0}\text{Im}\{\hat{n}\cdot[\vec{\alpha}^{-1} - \vec{\mathbf{S}}(k_{\parallel})]^{-1}\cdot\hat{n}\}$$

where the so-called lattice sum is defined by

$$\vec{\mathbf{S}}(k_{\parallel}) = \frac{k^2}{\varepsilon_r \varepsilon_0}\sum_{j\neq 0}\vec{\mathbf{G}}(0, \mathbf{r}_j, \omega)e^{-ik_{\parallel}\cdot r_j}$$

and $k_{\parallel}$ is the in-plane momentum of a particular Bloch mode. Lattice sums were efficiently and accurately evaluated using Ewald's method.[33,34]

Accurate polarizability tensors were determined numerically in a separate step for cylindrical NPs with the same geometric parameters as those used for the FDTD calculations. To do this, the scattered field $\mathbf{E}_s$ produced by an isolated cylinder excited by a plane wave was first calculated using the boundary-element method. A multipole decomposition[35] was then performed on $\mathbf{E}_s$ at each wavelength to determine the expansion coefficient values for a representation of $\mathbf{E}_s$ in terms of the vector spherical harmonics. The extracted a_1 scattering coefficient is related to the polarizability tensor element along the direction of the incident polarization by

$$\alpha = i\frac{6\pi\varepsilon_r\varepsilon_0}{k^3}a_1$$

The full polarizability tensor $\vec{\boldsymbol{\alpha}}$ is constructed by repeating this procedure for incident polarization directions along the long and short cylinder axes.

Linear Optical Property Measurements. The optical setup for transmission spectra measurements of finite NP lattices was adapted from a dark-field microscope (Nikon TE2000-U) by removing the condenser lens. Collimated white light was focused onto the sample with a spot size of ~50 μm by the objective lens (100×), and the transmission signals were split between the camera and the spectrometer for imaging and optical characterization, respectively. A narrow slit (width <1 μm) was inserted in front of the detector to ensure that the transmission signals collected from the sample are from the surface normal in spite of the large NA (variable between 0.5 and 1.3) of the objective lens.

Lasing Measurements from Finite NP Lattices. Finite NP lattices integrated with liquid dye IR-140 (dissolved in dimethyl sulfoxide) were pumped with a mode-locked Ti:sapphire laser with a regenerative amplifier (800 nm wavelength, 1 kHz operation rate, and 90 fs pulse width), and the pump spot was ~50 μm in diameter. An objective lens (10×, NA = 0.25) was used to focus the pulsed laser beam on the microscale lattice region, and the emission signals at the sample surface normal were collected by the same lens and redirected by the beam splitter. Lasing signals were then analyzed by a charge-coupled device (CCD) spectrometer (LN_2-cooled CCD/Triax 552, Horiba Jobin Yvon, ~0.15 nm resolution).

Finite-Difference Time-Domain Simulations. FDTD calculations with commercial software (FDTD Solution, Lumerical Inc., Vancouver, Canada) were used to model the linear optical properties and lasing emission from finite gold NP lattices. The optical constants of gold were taken from Johnson and Christy measurements (400−1000 nm).[36] A uniform mesh size of 4 nm (x, y, and z) was used to ensure the accuracy of electric and magnetic field calculations within the metal regions. To study lasing emission, a four-level one-electron model for describing dye molecules was integrated into FDTD. In the semiquantum system, we set the gold NP size at d = 130 nm and height h = 50 nm, dye concentration at C = 1 mM, pump wavelength at λ_a = 800 nm, and dye emission at λ_e = 860 nm. A perfectly matching layer was used as the boundary condition in simulations.

■ ASSOCIATED CONTENT

Supporting Information

The Supporting Information is available free of charge at https://pubs.acs.org/doi/10.1021/acsphotonics.0c00231.

Dependence of lattice plasmon resonances on nanoparticle number and diameter; coupled dipole modeling of finite lattices; scattering cross section plots for different-sized nanoparticles; evolution of hybrid quadrupole plasmons; distributions of the induced dipole moments; near fields of finite lattices; semiquantum modeling for plasmon lasing; dye concentration as a probe of the cavity losses; power-dependent lasing emission; dependence of lasing emission on transition lifetimes (PDF)

■ AUTHOR INFORMATION

Corresponding Authors

George C. Schatz − *Graduate Program in Applied Physics and Department of Chemistry, Northwestern University, Evanston, Illinois 60208, United States;* orcid.org/0000-0001-5837-4740; Email: g-schatz@northwestern.edu

Teri W. Odom − *Graduate Program in Applied Physics, Department of Chemistry, and Department of Materials Science and Engineering, Northwestern University, Evanston, Illinois 60208, United States;* orcid.org/0000-0002-8490-292X; Email: todom@northwestern.edu

Authors

Danqing Wang − *Graduate Program in Applied Physics, Northwestern University, Evanston, Illinois 60208, United States;* orcid.org/0000-0002-7369-1944

Marc R. Bourgeois − *Department of Chemistry, Northwestern University, Evanston, Illinois 60208, United States;* orcid.org/0000-0002-9435-9051

Jun Guan − *Graduate Program in Applied Physics, Northwestern University, Evanston, Illinois 60208, United States;* orcid.org/0000-0001-8667-1611

Ahmad K. Fumani − *Department of Chemistry, Northwestern University, Evanston, Illinois 60208, United States*

Complete contact information is available at: https://pubs.acs.org/10.1021/acsphotonics.0c00231

https://dx.doi.org/10.1021/acsphotonics.0c00231
ACS Photonics 2020, 7, 630−636

Author Contributions

D.W., G.C.S., and T.W.O. conceived the idea of finite nanoparticle lattice studies. D.W. fabricated the devices, carried out the optical measurements, and performed FDTD numerical simulations of the band structure, near-field distribution, and lasing actions of the system. M.R.B. carried out theoretical modeling based on the coupled dipole method. J.G. fabricated the finite lattice Si masters with e-beam lithography, and A.K.F. helped with the optical setup of lasing measurements. T.W.O. and G.C.S. guided experimental and theoretical investigations. D.W., M.R.B., G.C.S., and T.W.O. analyzed the data and wrote the manuscript. All authors commented on and revised the manuscript.

Notes

The authors declare no competing financial interest.

■ ACKNOWLEDGMENTS

This work was supported by the National Science Foundation (NSF) under DMR-1608258 and DMR-1904385 (D.W., G.C.S., T.W.O.) and the Vannevar Bush Faculty Fellowship from DOD under N00014-17-1-3023 (J.G., T.W.O.). Theoretical methods development (M.R.B., G.C.S.) was supported by the Department of Energy, Office of Basic Energy Science, under DE-SC0004752. This work utilized the Northwestern University Micro/Nano Fabrication Facility (NUFAB), which is partially supported by Soft and Hybrid Nanotechnology Experimental (SHyNE) Resource (NSF ECCS-1542205), the Materials Research Science and Engineering Center (DMR-1720139), the State of Illinois, and Northwestern University. This research was supported in part by the Quest high performance computing facility at Northwestern University, which is jointly supported by the Office of the Provost, the Office for Research, and Northwestern University Information Technology. We appreciate Tingting Liu and Thaddeus Reese for helpful discussions.

■ REFERENCES

(1) Willets, K. A.; Van Duyne, R. P. Localized Surface Plasmon Resonance Spectroscopy and Sensing. *Annu. Rev. Phys. Chem.* **2007**, *58*, 267−297.
(2) Sherry, L. J.; Chang, S. H.; Schatz, G. C.; Van Duyne, R. P.; Wiley, B. J.; Xia, Y. Localized Surface Plasmon Resonance Spectroscopy of Single Silver Nanocubes. *Nano Lett.* **2005**, *5*, 2034−2038.
(3) Kelly, K. L.; Coronado, E.; Zhao, L. L.; Schatz, G. C. The Optical Properties of Metal Nanoparticles: The Influence of Size, Shape, and Dielectric Environment. *J. Phys. Chem. B* **2003**, *107*, 668−677.
(4) Novotny, L.; van Hulst, N. Antennas for Light. *Nat. Photonics* **2011**, *5*, 83−90.
(5) Suh, J. Y.; Odom, T. W. Nonlinear Properties of Nanoscale Antennas. *Nano Today* **2013**, *8*, 469−479.
(6) Yang, A. K.; Huntington, M. D.; Cardinal, M. F.; Masango, S. S.; Van Duyne, R. P.; Odom, T. W. Hetero-Oligomer Nanoparticle Arrays for Plasmon-Enhanced Hydrogen Sensing. *ACS Nano* **2014**, *8*, 7639−7647.
(7) Fan, J. A.; Wu, C. H.; Bao, K.; Bao, J. M.; Bardhan, R.; Halas, N. J.; Manoharan, V. N.; Nordlander, P.; Shvets, G.; Capasso, F. Self-Assembled Plasmonic Nanoparticle Clusters. *Science* **2010**, *328*, 1135−1138.
(8) Kravets, V. G.; Schedin, F.; Grigorenko, A. N. Extremely Narrow Plasmon Resonances Based on Diffraction Coupling of Localized Plasmons in Arrays of Metallic Nanoparticles. *Phys. Rev. Lett.* **2008**, *101*, 087403.
(9) Zou, S.; Janel, N.; Schatz, G. C. Silver Nanoparticle Array Structures That Produce Remarkably Narrow Plasmon Lineshapes. *J. Chem. Phys.* **2004**, *120*, 10871−10875.
(10) Auguie, B.; Barnes, W. L. Collective Resonances in Gold Nanoparticle Arrays. *Phys. Rev. Lett.* **2008**, *101*, 143902.
(11) Wang, W.; Väkeväinen, A. I.; Törmä, P.; Rivas, J. G.; Odom, T. W. The Rich Photonic World of Plasmonic Nanoparticle Arrays. *Mater. Today* **2018**, *21*, 303.
(12) Wang, D.; Guan, J.; Hu, J.; Bourgeois, M. R.; Odom, T. W. Manipulating Light-Matter Interactions in Plasmonic Nanoparticle Lattices. *Acc. Chem. Res.* **2019**, *52*, 2997.
(13) Wang, D.; Wang, W.; Knudson, M. P.; Schatz, G. C.; Odom, T. W. Structural Engineering in Plasmon Nanolasers. *Chem. Rev.* **2018**, *118*, 2865−2881.
(14) Ebbesen, T. W.; Lezec, H. J.; Ghaemi, H. F.; Thio, T.; Wolff, P. A. Extraordinary Optical Transmission through Sub-Wavelength Hole Arrays. *Nature* **1998**, *391*, 667−669.
(15) Gao, H.; Hyun, J. K.; Lee, M. H.; Yang, J. C.; Lauhon, L. J.; Odom, T. W. Broadband Plasmonic Microlenses Based on Patches of Nanoholes. *Nano Lett.* **2010**, *10*, 4111−4116.
(16) Ogita, S.; Kotaki, Y.; Kihara, K.; Matsuda, M.; Ishikawa, H.; Imai, H. Dependence of Spectral Linewidth on Cavity Length and Coupling Coefficient in Dfb Laser. *Electron. Lett.* **1988**, *24*, 613−614.
(17) Ghafouri-Shiraz, H. *Distributed Feedback Laser Diodes and Optical Tunable Filters*; John Wiley: Chichester, England, 2003.
(18) Wang, D.; Yang, A.; Wang, W.; Hua, Y.; Schaller, R. D.; Schatz, G. C.; Odom, T. W. Band-Edge Engineering for Controlled Multi-Modal Nanolasing in Plasmonic Superlattices. *Nat. Nanotechnol.* **2017**, *12*, 889−894.
(19) Zhou, W.; Dridi, M.; Suh, J. Y.; Kim, C. H.; Co, D. T.; Wasielewski, M. R.; Schatz, G. C.; Odom, T. W. Lasing Action in Strongly Coupled Plasmonic Nanocavity Arrays. *Nat. Nanotechnol.* **2013**, *8*, 506−511.
(20) Yang, A.; Hoang, T. B.; Dridi, M.; Deeb, C.; Mikkelsen, M. H.; Schatz, G. C.; Odom, T. W. Real-Time Tunable Lasing from Plasmonic Nanocavity Arrays. *Nat. Commun.* **2015**, *6*, 6939.
(21) Fernandez-Bravo, A.; Wang, D.; Barnard, E. S.; Teitelboim, A.; Tajon, C.; Guan, J.; Schatz, G. C.; Cohen, B. E.; Chan, E. M.; Schuck, P. J.; Odom, T. W. Ultralow-Threshold, Continuous-Wave Upconverting Lasing from Subwavelength Plasmons. *Nat. Mater.* **2019**, *18*, 1172−1176.
(22) Hill, M. T.; Gather, M. C. Advances in Small Lasers. *Nat. Photonics* **2014**, *8*, 908−918.
(23) Ma, R. M.; Oulton, R. F. Applications of Nanolasers. *Nat. Nanotechnol.* **2019**, *14*, 12−22.
(24) Hakala, T. K.; Rekola, H. T.; Väkeväinen, A. I.; Martikainen, J.-P.; Nečada, M.; Moilanen, A. J.; Törmä, P. Lasing in Dark and Bright Modes of a Finite-Sized Plasmonic Lattice. *Nat. Commun.* **2017**, DOI: 10.1038/ncomms13687.
(25) Martikainen, J. P.; Moilanen, A. J.; Torma, P. Coupled Dipole Approximation across the Gamma-Point in a Finite-Sized Nanoparticle Array. *Philos. Trans. R. Soc., A* **2017**, *375*, 20160316.
(26) Zundel, L.; Manjavacas, A. Finite-Size Effects on Periodic Arrays of Nanostructures. *J. Phys.: Photonics* **2019**, *1*, 015004.
(27) Cherqui, C.; Bourgeois, M. R.; Wang, D.; Schatz, G. C. Plasmonic Surface Lattice Resonances: Theory and Computation. *Acc. Chem. Res.* **2019**, *52*, 2548.
(28) Manjavacas, A.; Zundel, L.; Sanders, S. Analysis of the Limits of the near-Field Produced by Nanoparticle Arrays. *ACS Nano* **2019**, *13*, 10682−10693.
(29) Wang, D.; Bourgeois, M. R.; Lee, W. K.; Li, R.; Trivedi, D.; Knudson, M. P.; Wang, W.; Schatz, G. C.; Odom, T. W. Stretchable Nanolasing from Hybrid Quadrupole Plasmons. *Nano Lett.* **2018**, *18*, 4549−4555.
(30) Henzie, J.; Lee, M. H.; Odom, T. W. Multiscale Patterning of Plasmonic Metamaterials. *Nat. Nanotechnol.* **2007**, *2*, 549−554.
(31) Li, R.; Wang, D.; Guan, J.; Wang, W.; Ao, X.; Schatz, G. C.; Schaller, R. D.; Odom, T. W. Plasmon Nanolasing with Aluminum Nanoparticle Arrays. *J. Opt. Soc. Am. B* **2019**, *36*, E104−E111.

https://dx.doi.org/10.1021/acsphotonics.0c00231
ACS Photonics 2020, 7, 630−636

(32) Wang, W.; Watkins, N.; Yang, A.; Schaller, R. D.; Schatz, G. C.; Odom, T. W. Ultrafast Dynamics of Lattice Plasmon Lasers. *J. Phys. Chem. Lett.* **2019**, *10*, 3301−3306.
(33) Linton, C. M. Lattice Sums for the Helmholtz Equation. *SIAM Rev.* **2010**, *52*, 630−674.
(34) Campione, S.; Capolino, F. Ewald Method for 3d Periodic Dyadic Green's Functions and Complex Modes in Composite Materials Made of Spherical Particles under the Dual Dipole Approximation. *Radio Sci.* **2012**, *47*, RS0N06.
(35) Grahn, P.; Shevchenko, A.; Kaivola, M. Electromagnetic Multipole Theory for Optical Nanomaterials. *New J. Phys.* **2012**, *14*, 093033.
(36) Johnson, P. B.; Christy, R. W. Optical Constants of Noble Metals. *Phys. Rev. B* **1972**, *6*, 4370−4379.

https://dx.doi.org/10.1021/acsphotonics.0c00231
ACS Photonics 2020, 7, 630−636